Anal. Bioanal. Electrochem., Vol. 17, No. 8, 2025, 696-720
https://www.doi.org/10.22034/abec.2025.733513

Analytical &
Bioanalytical
Electrochemistry

2025 by CEE
www.abechem.com

Full Paper

Experimental and Theoretical Study of Piper Nigrum Seed: Isolation of Piperine, DFT/MD Adsorption Modeling and Nano-formulation as a Green Corrosion Inhibitor for Carbon Steel in 1.0 M HCl

Suror W. Abduliridha,[1,2,*] K. Farhadi,[1] Reza E. Sabzi,[1] and A.S. Abdulnabi[2]

[1]*Department of Chemistry, Faculty of Science, Urmia University, Urmia, Iran*
[2]*Department of Chemistry, College of Education for Pure Sciences, University of Basrah, Basrah, Iraq*

*Corresponding Author, Tel.: +964-7734267652
E-Mails: Suror991@gmail.com ; s.waleedabdulridha@urmia.ac.ir

Received: 7 October 2025 / Received in revised form: 20 December 2025 /
Accepted: 20 December 2025 / Published online: 31 December 2025

Abstract- This study presents an integrated experimental and theoretical investigation into the corrosion inhibition of carbon steel in 1.0 M HCl using Piper nigrum seed extract and its poly(lactic-co-glycolic acid) or PLGA-based nanoformulation. Electrochemical analyses revealed that the nanoencapsulated system markedly suppressed anodic dissolution and cathodic hydrogen evolution, achieving inhibition efficiencies above 90% across a wide concentration range. Surface characterization via SEM, TEM, EDS, and FTIR confirmed the formation of a compact, adherent protective layer, with distinct shifts in C=O, C–O, and aromatic vibrational bands evidencing chemisorption of phytochemicals and polymer-assisted encapsulation. Complementary density functional theory (DFT) calculations and molecular dynamics (MD) simulations demonstrated strong electron donation, favorable adsorption geometry, and stable inhibitor–metal interactions with adsorption energies exceeding −170 kJ/mol. The combined findings establish a robust mechanistic basis for the inhibitor's performance, highlighting the synergistic benefits of phytochemical constituents and nanocarrier encapsulation. The results not only underscore the promise of Piper nigrum as an eco-friendly corrosion inhibitor but also demonstrate how nanoengineering strategies can advance green chemistry approaches to industrial corrosion mitigation.

Keywords- Piper nigrum extract; Poly(lactic-co-glycolic acid) nanoformulation; Green corrosion inhibitor; Electrochemical impedance spectroscopy; Potentiodynamic polarization; Density functional theory; Molecular dynamics simulation; Sustainable corrosion mitigation

1. INTRODUCTION

Corrosion is a multifaceted electrochemical phenomenon that originates at the metal–electrolyte boundary and progressively weakens the mechanical integrity of engineering structures. In the case of carbon steel, a widely used construction and industrial material, the problem becomes particularly critical in acidic environments where dissolution rates are accelerated [1-6]. Hydrochloric acid (HCl), commonly employed for industrial operations such as pickling, descaling, oil well acidification, and fertilizer production, is known to significantly intensify the degradation of steel surfaces [7]. Therefore, the development of reliable corrosion mitigation strategies is essential to preserve structural safety and reduce economic losses.

Traditional corrosion inhibitors, while often effective, suffer from serious drawbacks such as toxicity, high cost, and poor biodegradability [8]. In response to these limitations, the search for environmentally sustainable inhibitors has shifted attention toward plant-derived materials. Plant extracts are attractive candidates because they contain abundant organic compounds—such as alkaloids, tannins, flavonoids, and phenolics—rich in heteroatoms (O, N, S) and conjugated systems that enable strong adsorption on metallic surfaces [9]. These natural substances can form protective layers that suppress both anodic and cathodic reactions, thus lowering the corrosion rate while offering advantages including biodegradability, low toxicity, and economic feasibility [10]. However, certain limitations exist, including variations in chemical composition due to environmental factors, potential instability under harsh acidic conditions, and the need for relatively higher concentrations compared to synthetic inhibitors [11].

Recent investigations have provided compelling evidence of the anti-corrosive potential of natural extracts. For instance, the aqueous extract of *Pistia stratiotes* leaves demonstrated inhibition efficiencies exceeding 90% in 1 M HCl, supported by electrochemical impedance spectroscopy (EIS) and polarization measurements [12]. These findings highlight the ability of plant-based inhibitors to deliver high performance while complying with green chemistry principles. Also, Recent studies have expanded the scope of green corrosion inhibitors by examining a variety of plant-derived extracts under aggressive acidic conditions. For example, aqueous extracts of *Azadirachta indica* (neem) and *Lawsonia inermis* (henna) have shown inhibition efficiencies above 85% in 1 M HCl, with results confirmed through potentiodynamic polarization and electrochemical impedance spectroscopy (EIS) [13]. Similarly, alkaloid-rich extracts from *Capsicum annuum* demonstrated strong adsorption behavior on carbon steel surfaces, forming stable protective films that significantly reduced the corrosion rate [14]. These findings not only reinforce the versatility of natural extracts as sustainable alternatives to synthetic inhibitors but also emphasize the critical role of heteroatom-containing compounds and polyphenols in enhancing surface coverage and minimizing charge transfer processes. Collectively, the results highlight a clear trend toward the integration of eco-friendly inhibitors into industrial corrosion management strategies, aligning performance with the principles of sustainability and green chemistry.

Within this framework, *Piper nigrum* (black pepper) seed extract has emerged as a promising green inhibitor. It is chemically enriched with alkaloids such as piperine, which possess multiple functional groups capable of coordinating with steel surfaces to improve adsorption and enhance protective film stability [15-22]. In addition to its wide availability and non-toxic nature, its chemical reactivity aligns well with the requirements of eco-friendly corrosion prevention.

The present work introduces a novel contribution by combining experimental and theoretical approaches to elucidate the corrosion inhibition mechanism of Piper nigrum seed aqueous extract on carbon steel in 1.0 M HCl. Electrochemical techniques, including EIS and potentiodynamic polarization, complemented by surface analysis and computational modeling, are employed to elucidate the adsorption mechanism and quantify its efficiency. Theoretical insights are strengthened by integrating density functional theory (DFT) calculations with molecular dynamics simulations to model the adsorption orientation, stability, and interaction energies of extract molecules on steel surfaces. Theoretical interpretation is reinforced through combined density functional theory (DFT) and molecular dynamics simulations, which describe adsorption geometry, interaction strength, and film stability at the steel–solution interface. In parallel, a nanoformulation strategy is introduced to enhance the stability and sustained release of the active extract, offering improved surface coverage compared to conventional crude preparations. This research highlights a novel strategy by isolating the active constituents of Piper nigrum and incorporating them into a nanoformulated system to enhance stability and release control. Supported by density functional theory and molecular dynamics simulations alongside advanced surface analyses, the study delivers mechanistic insight into adsorption and protection processes. The combined approach establishes a practical and environmentally sustainable pathway for applying green inhibitors to carbon steel in acidic environments.

2. EXPERIMENTAL SECTION

2.1. Preparation and Nanoformulation of Piper nigrum Inhibitors

In this work, Piper nigrum seeds were employed as the natural precursor of green corrosion inhibitors. Prior to extraction, the seeds were thoroughly rinsed with distilled water, oven-dried to eliminate residual moisture, and finely milled into a uniform powder to maximize surface area exposure. Approximately 10 g of the prepared seed powder was carefully loaded into a cellulose thimble and subjected to Soxhlet reflux using 300 mL of distilled water as the extraction medium. The process was conducted at a controlled temperature range of 80–90 °C for a period of 12–48 h to ensure efficient transfer of phytoconstituents into the solvent phase. Upon completion, the aqueous extract was filtered and concentrated under reduced pressure using a rotary evaporator to remove the excess solvent. The concentrated material was subsequently air-dried at ambient temperature, yielding a stable aqueous extract that was stored in airtight containers until further experimental investigations [22,23]. To enhance the stability and achieve a controlled release profile, the crude aqueous extract was incorporated into a nanocarrier system. Nanoencapsulation was carried out using a nanoprecipitation approach, where the extract was dispersed in an ethanol–water mixture containing poly(lactic-co-glycolic acid) (PLGA, 50:50 lactic/glycolic ratio; Mw ≈ 30-60 kDa) as a biodegradable polymeric matrix. Ultrasonication was applied for 20 minutes to promote efficient entrapment of the bioactive constituents and to reduce particle size to the nanometer scale. The resulting suspension was subsequently centrifuged at 12000 rpm for 30 minutes, washed thoroughly with deionized water to eliminate residual free molecules, and finally lyophilized to obtain a stable, free-flowing nanomaterial. Both the purified phytoconstituents (notably piperine) and the PLGA-encapsulated extract were stored at 4°C in airtight containers until further electrochemical and surface characterization experiments were performed.

2.2. Surface Characterization of Carbon Steel

To assess the corrosion inhibition performance of *Piper nigrum* extract and its nanoformulation on N-80 carbon steel, surface morphology and composition were analyzed before and after immersion in 1.0 M HCl, both in the presence and absence of inhibitors. Prior to treatment, steel specimens were polished sequentially with silicon carbide papers (400–1200 grit), degreased with ethanol, rinsed with distilled water, and dried under ambient conditions. For inhibitor application and electrochemical testing, the specimens were immersed in 50 mL of inhibitor solutions at predetermined concentrations (10, 20, 30, 40, and 50 ppm for the nanoformulated extract) for 24 h at 25, 35, and 45 °C under static conditions. Following the immersion period and completion of electrochemical measurements, the samples were gently rinsed with distilled water, dried, and immediately subjected to surface characterization. Control specimens were immersed in 1.0 M HCl without inhibitors for comparison.

Surface features and microstructure were examined using scanning electron microscopy (SEM, JEOL JSM-7610F) to identify corrosion-induced defects, pits, and roughness. Transmission electron microscopy (TEM, Tecnai G2 F20) was employed to evaluate nanocapsule distribution and adhesion on the specimens. Energy-dispersive X-ray spectroscopy (EDS) coupled with SEM provided elemental composition and mapping, confirming the presence of adsorbed phytochemicals. Fourier-transform infrared spectroscopy (FTIR, Bruker Tensor 27) was used to identify characteristic functional groups and assess potential interactions between the inhibitors and the steel surface.

All analyses were conducted in triplicate to ensure reproducibility and enable statistical comparison of inhibition efficiency. This integrated approach, combining controlled inhibitor application with advanced surface-sensitive techniques, allows a detailed correlation between the physicochemical properties of the inhibitors and their effectiveness in mitigating corrosion under acidic conditions.

2.3. Experimental procedure for PPC and EIS measurements

The inhibitory action of the studied inhibitors was assessed over a range of concentrations in 1.0 M HCl at temperatures of 25, 35, and 45 °C by employing potentiodynamic polarization curve (PPC) analysis. Polarization experiments were conducted on N-80 grade carbon steel within a potential window of –250 to +250 mV relative to the open-circuit potential, using a constant scan rate of 1 mV s^{-1}. A conventional three-electrode corrosion cell was utilized, containing 1000 mL of test solution, with an Ag/AgCl electrode serving as the reference. From the obtained Tafel curves, the principal electrochemical parameters—including corrosion potential (E_{corr}) and corrosion current density (I_{corr})—were extracted. Based on these data, the inhibition efficiency (η%), surface coverage (θ), and potential displacement (ΔE_{corr}) were determined using Equations (1)–(3). Complementary electrochemical impedance spectroscopy (EIS) measurements were also performed to validate the PPC findings and provide further insight into the charge transfer resistance and double-layer capacitance of the inhibited system [24].

$$\%\,\boldsymbol{IE} = \left(\frac{I^{\circ}corr - Icorr}{I^{\circ}corr}\right) \times \mathbf{100} \qquad \textbf{(1)}$$

$$\boldsymbol{\Theta} = \left(\frac{I^{\circ}corr - Icorr}{I^{\circ}corr}\right) \qquad \textbf{(2)}$$

Where $I^{\circ}_{\mathbf{corr}}$ and $I_{\mathbf{corr}}$ are corrosion current densities in the absence and presence of an inhibitor, respectively.

$$\boldsymbol{\Delta E_{corr} = E_{corr\ inh} - E^{\circ}_{corr}} \qquad \textbf{(3)}$$

Where E_{corr} and E°_{corr} denoted the corrosion potential with and without inhibitor, respectively.

The inhibitor was tested at concentrations of 10, 20, 30, 40, and 50 ppm during the electrochemical impedance spectroscopy (EIS) measurements, which were performed at 25 °C in a 1.0 M HCl solution. Electrochemical analyses were carried out in a conventional three-electrode cell using a perturbation voltage of 20 mV relative to the open-circuit potential, with frequencies ranging from 10 Hz to 1000 Hz .The EIS parameters obtained included the charge transfer resistance (R_{ct}), solution resistance (R_s), and double-layer capacitance (C_{dl}).The values of Rs and R_{ct} were determined by extrapolating the high- and low-frequency intercepts of the fitted semicircular Nyquist plot on the real axis (Z_{real}), using an electrochemical corrosion analyzer. The double-layer capacitance (C_{dl}) was calculated according to Equation 4 [25], and the inhibition efficiency (%) of the inhibitor was evaluated using Equation 5 [25].

$$\boldsymbol{C_{dl} = \frac{1}{\omega \cdot R_{ct}}} \qquad \textbf{(4)}$$

where ω is the angular frequency which equals $2\pi f_{max}$. Here, the fmax is the frequency in Hz.

$$\boldsymbol{IE\%_{(EIS)} = \frac{R_{Ct(inh)} - R_{Ct(uninh)}}{R_{Ct(inh)}} . 100\%} \qquad \textbf{(5)}$$

The $R_{ct(inh)}$ and $R_{ct(uninh)}$ are the charge transfer resistance of the inhibited and uninhibited solution, respectively. The R'_{Ct} represents the charge transfer resistance with diffusion layer resistance which was calculated as described in Equation 6 [26].

$$\boldsymbol{R'_{Ct} = R_{Ct} - R_S} \qquad \textbf{(6)}$$

2.4. Experimental procedure for Molecular Dynamics (MD) Simulation

Molecular dynamics (MD) simulations were performed to provide atomistic insight into the adsorption behavior of the inhibitor molecules on carbon steel surfaces. The MD simulations were performed using the canonical NVT ensemble using a time step of 1 fs and a total simulation time of 100–500 ps at a constant temperature of 298 K, controlled by a Nosé–Hoover thermostat to ensure proper thermal equilibration. System equilibration was achieved within the first 20–30 ps, after which the total energy profile stabilized, indicating a dynamically equilibrated inhibitor–metal interface [2]. Throughout the simulation, the inhibitor molecule remained firmly adsorbed on the metal surface, with an average adsorption distance of 2.1–2.4 Å between heteroatom active sites and surface atoms. Periodic boundary conditions were applied in all three spatial directions to eliminate edge effects. The metallic substrate was modeled as a crystalline Fe(110) slab composed of six atomic layers, with the bottom two layers fixed to mimic bulk constraints and the upper layers allowed to relax dynamically. The inhibitor molecules (piperine and PLGA-encapsulated piperine) were initially positioned parallel to the Fe(110) surface at a distance of ~5 Å and immersed in an explicit aqueous environment containing water molecules and chloride ions to replicate realistic acidic conditions. Periodic boundary conditions were applied in all three spatial directions to eliminate edge effects.

The COMPASS force field was employed for all atomistic interactions due to its proven accuracy in describing organic–metal and metal–solvent systems. Long-range electrostatic interactions were calculated using the Ewald summation method, while van der Waals interactions were treated using an atom-based cutoff of 12 Å.

Energy minimization was first conducted using the steepest descent algorithm until the force convergence criterion of 1×10^{-4} kcal·mol^{-1}·Å^{-1} was achieved. Subsequently, the system was equilibrated for 30 ps, followed by a production run of 500 ps with an integration time step of 1 fs. The total energy and temperature profiles stabilized within the initial equilibration stage, indicating attainment of dynamic equilibrium.

3. RESULTS AND DISCUSSION

3.1. Potentiodynamic Polarization Curves (PPC)

Initially, carbon steel was exposed to a concentration of 5 ppm of both the purified phytoconstituents and the PLGA-encapsulated extract, and the corresponding Tafel and impedance plots were obtained, as presented in Figure 1. The comparative analysis of the polarization curves reveals that the PLGA-encapsulated extract exhibits superior corrosion inhibition performance compared to the purified phytoconstituents extract. Specifically, the PLGA-based inhibitor demonstrates a more positive corrosion potential (E_{corr}) and a significantly lower corrosion current density (I_{corr}), indicating a reduced rate of electrochemical degradation. This shift in E_{corr} suggests enhanced thermodynamic stability of the metal surface, while the decrease in I_{corr} reflects improved kinetic resistance to anodic and cathodic reactions. The encapsulation within PLGA likely facilitates sustained release and better surface coverage, contributing to its enhanced protective behavior.

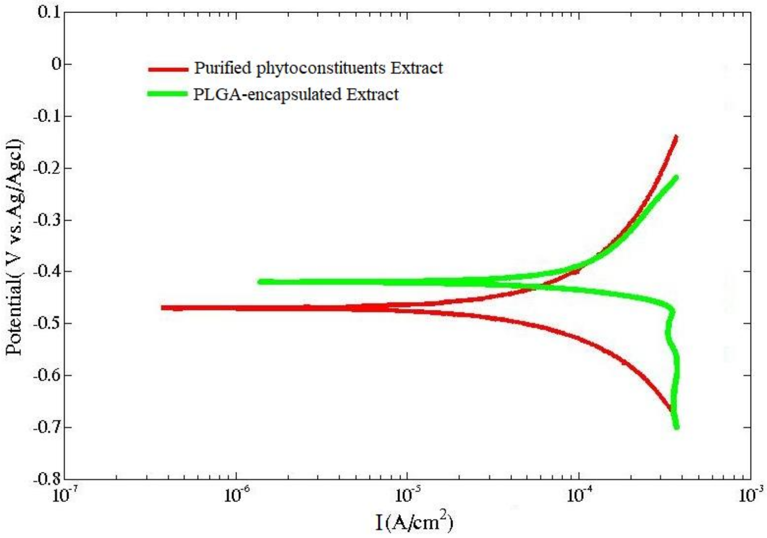

Figure 1. Tafel plots for carbon steel alloy in the 40 ppm concentration of the purified phytoconstituents and the PLGA-encapsulated extract inhibitors in the aqueous solution of hydrochloric acid (1.0 M)

These findings underscore the potential of PLGA-based systems as effective corrosion inhibitors compared with the purified phytoconstituents extract inhibitor. Therefore, further investigations will be focused on the PLGA-encapsulated extract due to its superior electrochemical performance, as evidenced by its more positive corrosion potential and lower corrosion current density. These findings suggest that PLGA encapsulation enhances the inhibitor's protective efficiency, making it a promising candidate for advanced corrosion control strategies.

The corrosion rate of carbon steel was measured in an aqueous solution of hydrochloric acid at temperatures of 25, 35, and 45°C in the presence of PLGA-encapsulated extract inhibitor at concentrations ranging from 10 to 50 ppm, using potentiodynamic polarization (Tafel plot). Each of the corrosion potential (E_{corr}), corrosion current density (I_{corr}), corrosion rate (CR), and potential displacement (ΔE_{corr}) was recorded [27].

3.2. Investigation of the Corrosion Rate Using PLGA-Encapsulated Extract Inhibitor at 25°C

The electrochemical behavior of stainless steel in the presence of different concentrations of PLGA-Encapsulated was investigated at 25°C. Figure 2 presents the potentiodynamic polarization curves for the blank solution and inhibitor concentrations ranging from 10 to 50 ppm. The corresponding electrochemical parameters, including corrosion potential (E_{corr}), corrosion current density (I_{corr}), corrosion rate (CR), anodic and cathodic Tafel slopes (B_a and B_c), inhibition efficiency (%IE), and surface coverage (θ), are summarized in Table 1.

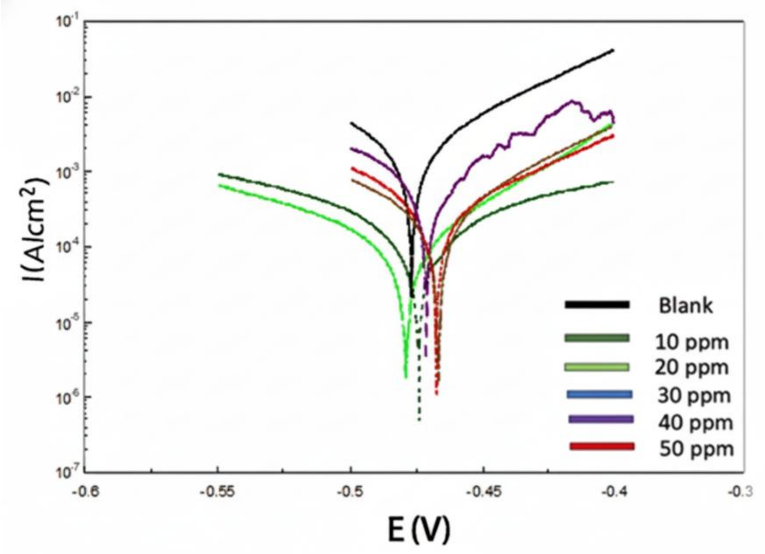

Figure 2. Tafel plots for carbon steel alloy in different concentrations of PLGA-Encapsulated Extract inhibitor in the aqueous solution of hydrochloric acid (1.0 M) at 25 °C

The blank sample exhibited a corrosion potential of -0.467 V and a corrosion current density of 3.60×10^{-4} A/cm², corresponding to a corrosion rate of 4.227 mm/year. Upon the addition of the inhibitor, a clear shift of E_{corr} towards more negative values was observed, indicating a mixed-type inhibition behavior with a slight cathodic predominance. Specifically, at 10 ppm, E_{corr} shifted to -0.479 V, while I_{corr} decreased to 2.521×10^{-4} A/cm², resulting in an inhibition efficiency of 30%.

Table 1. The corrosion parameters for carbon steel alloy in different concentrations of PLGA-Encapsulated Extract inhibitor in aqueous solution of hydrochloric acid (1 M) at 25°C

Inhibitor Conc (ppm)	E_{corr} (V)	CR (mm/y)	I_{corr} (A/cm^2)	B_a (mv)	B_c (mv)	(IE) %	θ
Blank	-0.467	4.227	3.601×10^{-4}	64.064	87.165	0	0
10	-0.479	3.121	2.521×10^{-4}	419.990	870.460	30.00	0.30
20	-0.474	2.968	1.211×10^{-4}	955.020	1242.700	66.38	0.66
30	-0.467	1.590	8.471×10^{-5}	61.502	99.483	76.47	0.76
40	-0.468	0.048	4.056×10^{-5}	67.289	102.760	88.75	0.88
50	-0.469	0.005	2.691×10^{-5}	33116	42959	92.52	0.93

Increasing the inhibitor concentration led to a continuous decrease in I_{corr} and corrosion rate, reflecting the enhanced surface coverage by the inhibitor molecules. Notably, the maximum inhibition was achieved at 50 ppm, with I_{corr} reaching 2.691×10^{-5} A/cm² and an inhibition efficiency of 92.52%, indicating nearly complete coverage of the steel surface ($\theta=0.925$).

The polarization curves (Figure 2) support these findings, showing a significant reduction in both anodic and cathodic currents with increasing inhibitor concentration. The anodic Tafel slope (B_a) increased from 64.064 mV/dec (blank) to 33116 mV/dec (50 ppm), and the cathodic slope (B_c) also exhibited a marked increase, demonstrating effective suppression of both anodic metal dissolution and cathodic hydrogen evolution reactions. Overall, the results clearly indicate that PLGA-Encapsulated extract exhibits excellent corrosion inhibition performance for stainless steel in the tested environment. The efficiency increases with concentration, achieving near-complete surface protection at 50 ppm, highlighting the potential of this inhibitor for practical applications in corrosion mitigation [27,28].

3.3. Investigation of the Corrosion Rate Using PLGA-Encapsulated Extract Inhibitor at 35°C

According to Figure 3 and Table 2, The electrochemical results clearly demonstrate that the presence of the inhibitor significantly suppresses the corrosion rate of steel. In the uninhibited system, the corrosion rate reached 50.56 mm/y with a corresponding corrosion current density of 2.69×10^{-3} A/cm². Upon the addition of 10 ppm inhibitor, a moderate decrease was observed, with the corrosion rate reduced to 40.56 mm/y and an inhibition efficiency of about 29%. A further increase in concentration to 20 ppm markedly lowered the corrosion rate to 2.29 mm/y, corresponding to an efficiency above 65%. At 30 ppm, the corrosion rate dropped to 0.137 mm/y with an efficiency of nearly 75%. The protective effect became more pronounced at higher concentrations, as 40 ppm decreased the corrosion rate to 0.027 mm/y (85.5% efficiency), while the maximum performance was achieved at 50 ppm, where the corrosion rate fell dramatically to 0.0096 mm/y, representing an inhibition efficiency of more than 91%.

Table 2. The corrosion parameters for carbon steel alloy in different concentrations of PLGA-Encapsulated Extract inhibitor in aqueous solution of hydrochloric acid (1 M) at 35°C

Inhibitor Conc (ppm)	E_{corr} (V)	CR (mm/y)	I_{corr} (A/cm^2)	B_a (mv)	B_c (mv)	(IE) %	θ
Blank	-0.471	50.567	2.691×0^{-3}	106.86	114.54	0	0
10	-0.396	40.560	1.900×10^{-3}	563.26	933.48	29.36	0.29
20	-0.402	2.287	9.170×10^{-4}	1207.80	1894	65.91	0.65
30	-0.438	0.137	6.800×10^{-4}	109.83	68.58	74.72	0.74
40	-0.419	0.027	3.940×10^{-4}	55.95	90.67	85.50	0.85
50	-0.445	0.009	2.280×10^{-4}	655	306.61	91.52	0.91

These quantitative findings confirm that the inhibitor exhibits a concentration-dependent performance, providing highly effective protection against steel corrosion at elevated dosages. The Δ_{Ecorr} data shows that the maximum potential displacement is 76 mV at 10 ppm, which is significantly less than 85 mV. Therefore, the potential displacement indicates that the PLGA-Encapsulated Extract Inhibitor influences both anodic and cathodic reactions. Therefore, PLGA-Encapsulated Extract Inhibitor can be considered a mixed-type inhibitor as evident in Figure 3.

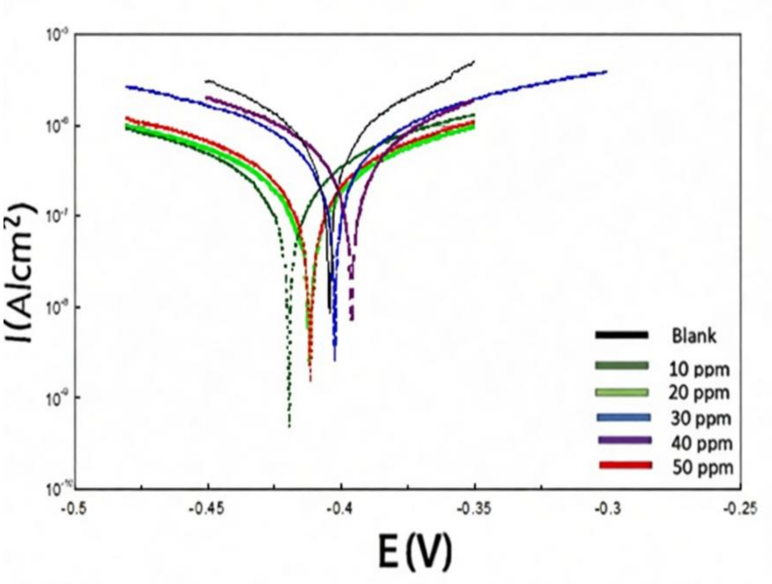

Figure 3. Tafel plots for carbon steel alloy in different concentrations of PLGA-Encapsulated Extract inhibitor in the aqueous solution of hydrochloric acid (1.0 M) at 35°C

The comparative evaluation of the electrochemical behavior at 25°C and 35°C reveals that temperature plays a critical role in accelerating the corrosion process. The higher corrosion rate at 35°C in the absence of inhibitor (50.56 mm/y versus 4.227 mm/y at 25°C) can be attributed to the enhanced mobility of ionic species, faster diffusion of aggressive chloride ions toward the steel surface, and the increased kinetics of both anodic dissolution and cathodic hydrogen evolution reactions. Elevated temperature also weakens the stability of the passive film, thereby facilitating easier charge transfer and accelerating corrosion reactions.

Despite this thermally induced acceleration, the PLGA-encapsulated extract inhibitor exhibited strong concentration-dependent inhibition efficiency at both temperatures. The encapsulation within PLGA ensures a controlled and gradual release of active molecules, allowing for effective adsorption on the steel surface even under elevated temperature conditions. The adsorption leads to the formation of a protective barrier that suppresses both anodic metal dissolution and cathodic hydrogen reduction, as confirmed by the shift in Tafel slopes and the potential displacement values ($\Delta E_{corr} < 85$ mV), which are characteristic of mixed-type inhibitors. At 25°C, inhibition efficiency reached 92.5% at 50 ppm, whereas at 35°C, efficiency remained above 91% at the same concentration, demonstrating the thermal robustness of the system. The nearly complete surface coverage ($\theta \approx 0.9$) highlights the ability of PLGA-encapsulated molecules to overcome thermal agitation and maintain strong adsorption on the steel surface. This dual functionality—thermal stability combined with mixed-type inhibition—suggests that the encapsulated extract not only counteracts the inherent acceleration of corrosion at higher temperatures but also provides reliable and sustainable protection, making it a promising candidate for practical anti-corrosion applications in environments with fluctuating thermal conditions [29].

3.4. Investigation of the Corrosion Rate Using PLGA-Encapsulated Extract Inhibitor at 45°C

Table 3 and Figure 3 show the Tafel curves for the corrosion of carbon steel alloy in an aqueous solution of hydrochloric acid without inhibitor compared with the Tafel curve in the presence of PLGA-Encapsulated Extract inhibitor at different concentrations. In the absence of an inhibitor, the corrosion rate reached approximately 177.2 mm/y with a corresponding corrosion current density of 1.63×10^{-3} A/cm^2, indicating severe degradation of the steel surface. Upon the addition of only 10 ppm of inhibitor, the corrosion rate was nearly halved, achieving an inhibition efficiency of about 23.5%. A further increase in concentration to 20 and 30 ppm led to a pronounced improvement, where the corrosion rate sharply decreased to 1.11 mm/y and subsequently to 0.035 mm/y, accompanied by efficiencies of 56.4% and 62.1%, respectively. At higher concentrations (40 and 50 ppm), the protective effect became even more remarkable, with the corrosion rate approaching negligible values (0.022 mm/y and 0.001 mm/y) and the inhibition efficiency rising to 81.5% and 88.7%, respectively. These results clearly demonstrate that the progressive increase in inhibitor concentration significantly suppresses both the corrosion current density and corrosion rate, thereby providing substantial protection to the steel surface. The ΔE_{corr} data indicate a maximum potential displacement of 21 mV at 50 ppm, which is significantly less than 85 mV, suggesting that the inhibitor controls both anodic and cathodic reactions. Therefore, PLGA-encapsulated extract inhibitor can be considered a mixed-type inhibitor as evident in Figure 4 [29].

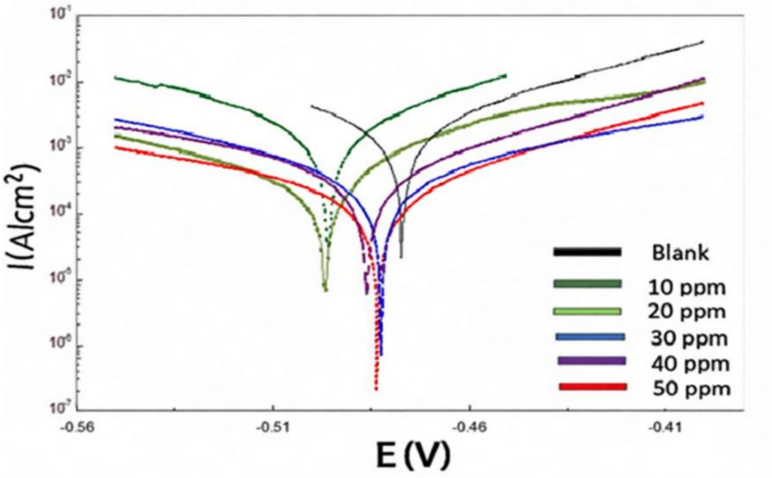

Figure 4. Tafel plots for carbon steel alloy in different concentrations of PLGA-Encapsulated Extract inhibitor in the aqueous solution of hydrochloric acid (1.0 M) at 45°C

Table 3. The corrosion parameters for carbon steel alloy in different concentrations of PLGA-Encapsulated Extract inhibitor in aqueous solution of hydrochloric acid (1 M) at 45°C

Inhibitor Conc (ppm)	E_{corr} (V)	CR (mm/y)	I_{corr} (A/cm^2)	B_a (mv)	B_c (mv)	(IE) %	θ
Blank	-0.477	177.200	1.630×10^{-3}	66.36	74.39	0	0
10	-0.476	72.402	12.460×10^{-4}	361.37	808.22	23.55	0.23
20	-0.460	1.110	7.110×10^{-4}	309.34	452.11	56.38	0.56
30	-0.477	0.035	6.170×10^{-4}	94.98	73.87	62.14	0.62
40	-0.463	0.022	3.010×10^{-4}	65.05	80.98	81.53	0.81
50	-0.455	0.001	1.840×10^{-4}	751.67	276.30	88.71	0.88

3.5. Electrochemical Impedance Spectroscopy (EIS) Investigation of Corrosion Inhibition

In order to evaluate the protective performance of the PLGA-encapsulated extract inhibitor, electrochemical impedance spectroscopy (EIS) measurements were carried out in 1 M HCl solution at 25°C, and related data are presented in Table 4. The Nyquist plots (Figure 5) revealed distinct semicircular capacitive loops, whose diameters increased progressively with higher inhibitor concentrations. In the absence of an inhibitor, the curve exhibited the smallest arc, corresponding to a low charge transfer resistance (R_{ct} = 16.98 Ω·cm²) and a high double-layer capacitance (C_{dl} = 168.8 μF/cm²), which indicates severe charge transfer and rapid corrosion. With the addition of only 10 ppm inhibitor, R_{ct} nearly doubled to 31.36 Ω·cm², yielding an inhibition efficiency of 45.9%. At intermediate concentrations (20–30 ppm), R_{ct} values continued to rise markedly (51.14–72.72 Ω·cm²) with corresponding efficiencies of 66.8% and 76.7%, demonstrating the enhanced blocking of active sites by adsorbed inhibitor molecules.

Table 4. Results of EIS for carbon steel alloy in different concentrations of PLGA-Encapsulated Extract inhibitor in aqueous solution of hydrochloric acid (1 M) at 25°C

Conc. (ppm)	f_{max} (Hz)	C_{dl} (μF/cm²)	R_{ct} (Ω·cm²)	R_s (Ω·cm²)	R' (Ω·cm²)	(IE) %	θ
0	50.20	168.80	16.98	0.018	16.96	0	0
10	40.07	126.72	31.36	0.033	31.32	45.86	0.45
20	30.18	103.17	51.14	0.053	51.08	66.80	0.66
30	25.30	86.54	72.72	0.075	72.64	76.66	0.76
40	22.30	74.38	94.30	0.098	94.20	81.94	0.81
50	20.70	63.57	121	0.120	120.80	85.97	0.85

A further increase to 40 ppm resulted in 94.30 Ω·cm², while the maximum concentration of 50 ppm provided the most significant improvement, raising R_{ct} to 121.0 Ω·cm² and achieving an efficiency of 85.97%. Simultaneously, C_{dl} values decreased systematically from 168.8 μF/cm² to 63.57 μF/cm², suggesting the formation of a compact and adherent protective film that reduced the dielectric constant and/or increased the thickness of the electrical double layer. These observations support the notion that the inhibitor molecules gradually displaced water molecules at the steel surface, leading to effective adsorption, enhanced barrier properties, and a substantial reduction in the corrosion rate [30-36].

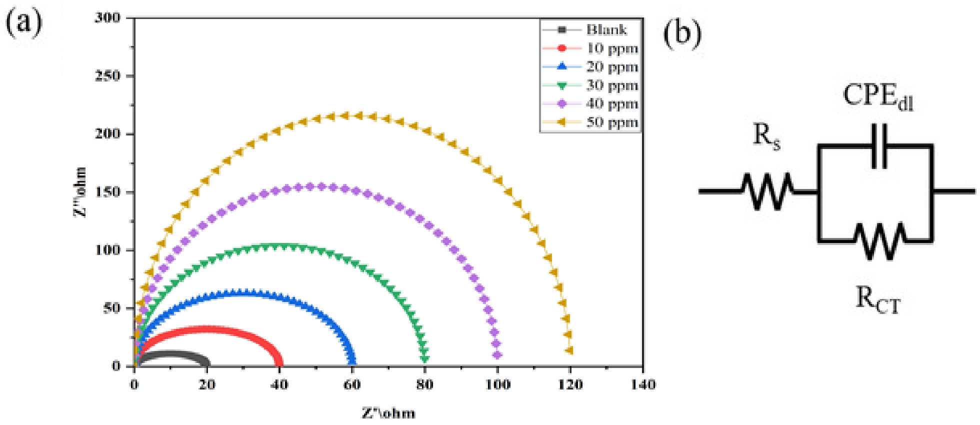

Figure 5. a) Typical Nyquist plots for carbon steel alloy in the different concentration of PLGA-Encapsulated Extract inhibitor in the aqueous solution of hydrochloric acid (1.0 M) b) Equivalent electrical circuit model used to fitting the Nyquist impedance response of the system, The model includes solution resistance (R_s), charge transfer resistance (R_{ct}), and constant phase element (CPE_{dl}) representing the double layer capacitance.

3.6. Surface Characterization and Morphological Analysis of Carbon Steel

In order to validate the protective performance of Piper nigrum extract and its PLGA nanoformulation, a set of surface-sensitive characterizations was conducted. In Figure 6a, SEM micrographs of untreated carbon steel revealed severe surface deterioration with dense pits and irregular cracks caused by acid attack, whereas samples exposed to the inhibitor displayed significantly smoother morphologies (Figure 6b), with the nanoformulated system showing an almost continuous protective layer as illustrated in Figure 6c. In other words, SEM micrographs reveal that the untreated steel surface is severely damaged by pits and cracks, whereas inhibitor-treated samples exhibit smoother morphologies with markedly reduced defects; in particular, the nanoencapsulated system forms a more uniform protective layer. TEM analysis in Figure 6d,e, confirmed the successful synthesis of spherical PLGA nanocapsules (50–200 nm) encapsulating the phytochemicals with well-defined boundaries and strong dispersion, validating efficient encapsulation of the bioactive extract, which adhered strongly to the steel surface, thereby enhancing coverage and uniformity. Zoomed-in image highlighting core–shell structure and size distribution.

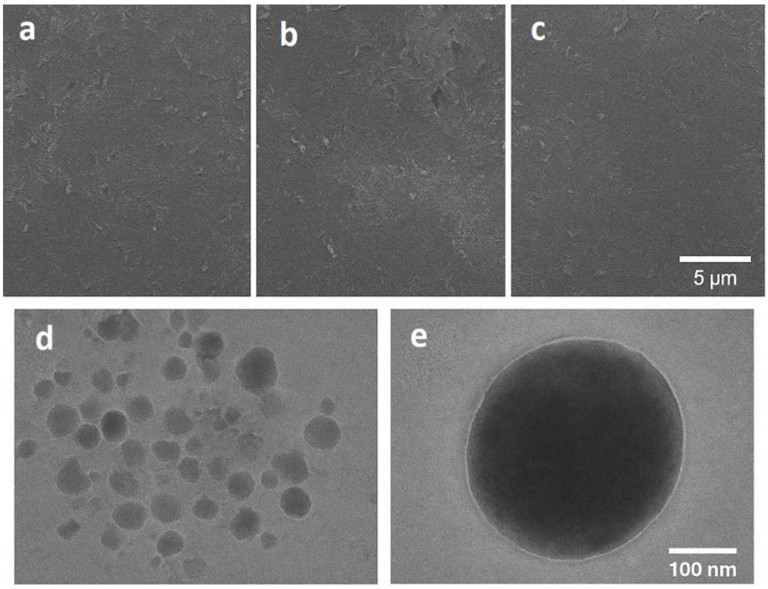

Figure 6. Characterization of corrosion inhibition by Piper nigrum extract and its PLGA nanoformulation: (a-c) SEM images of carbon steel surfaces before and after inhibitor treatment, (d,e) TEM images of spherical PLGA nanocapsules

The EDS elemental maps in Figure 7, provide a direct visualization of the surface chemistry of carbon steel before and after immersion in 1.0 M HCl with Piper nigrum extract and its nanoformulation. In the control sample, Fe and Cl signals dominate, confirming severe chloride adsorption and localized corrosion sites, while C intensity remains minimal, consistent with the absence of organic coverage. In contrast, the inhibited sample displays a significant decrease in Cl distribution accompanied by a pronounced increase in C and O signals, indicating strong adsorption of phytoconstituents and the presence of oxygen-rich functional groups from PLGA nanocapsules. In other words, EDS elemental mapping highlights reduced chloride and enhanced carbon signatures on protected surfaces, indicating successful adsorption of phytochemicals and suppression of corrosive species.

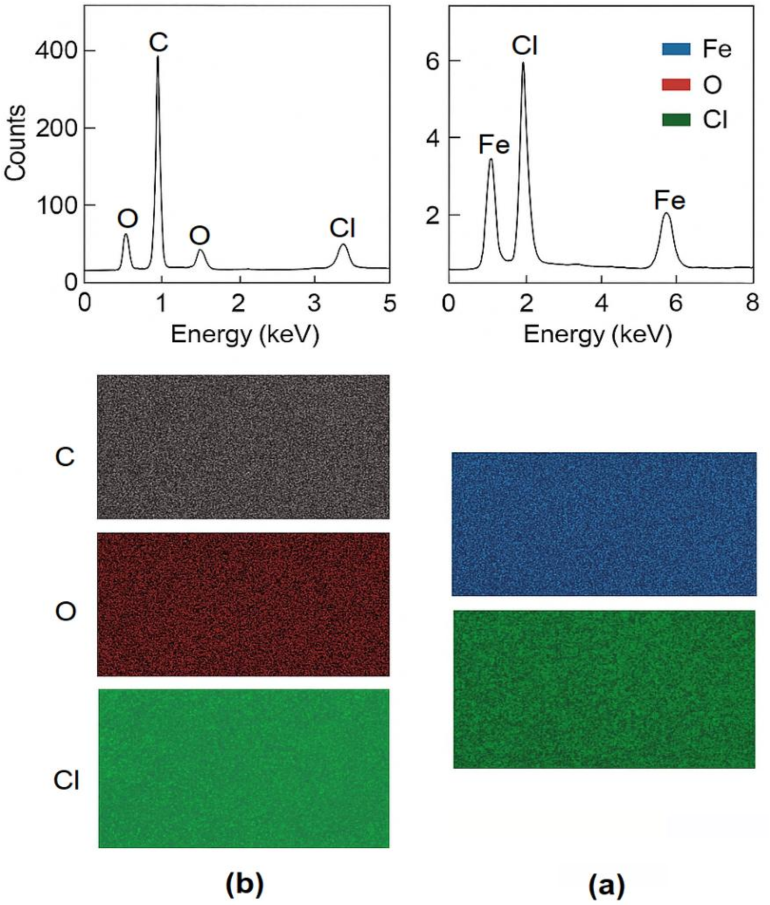

Figure 7. EDS elemental distribution maps of carbon steel surfaces: (a) control specimen after immersion in 1.0 M HCl, showing intense Fe and Cl signals, (b) inhibited specimen treated with Piper nigrum nanoformulation, showing increased C and O and reduced Cl intensity

FTIR spectra in Figure 8, provided complementary evidence, where the characteristic vibrations of C=O, C–O, and aromatic groups shifted upon interaction with the metal, confirming chemisorption, while additional ester bands verified the presence of PLGA in the encapsulated system. The FTIR spectra of carbon steel treated with Piper nigrum extract and its PLGA nanoformulation reveal clear and well-resolved peaks, demonstrating successful adsorption and encapsulation of the bioactive compounds on the metal surface. The peaks at 3000–2850 cm^{-1} are attributed to C–H stretching of aliphatic chains present in both the extract and the PLGA matrix. A pronounced absorption at 1750 cm^{-1} is characteristic of C=O stretching from ester functionalities of PLGA, whereas the band near 1650 cm^{-1} reflects C=O and aromatic stretching vibrations, confirming chemisorption of phytochemicals onto the steel surface. The peaks at 1500–1400 cm^{-1} arise from C=C aromatic stretching of the extract constituents, while those at 1300–1200 cm^{-1} and 1100–1050 cm^{-1} correspond to C–O stretching of esters and ether linkages, indicating successful polymeric encapsulation. Compared to bare steel, the nanoformulated system exhibits enhanced band intensity, demonstrating superior surface coverage and the formation of a uniform protective layer that underpins its high inhibition efficiency. Collectively, the FTIR data establish a clear correlation between the morphological, compositional, and spectroscopic evidence and the high inhibition efficiency observed electrochemically, supporting the role of the nanoengineered extract as a robust and sustainable corrosion inhibitor [37,38].

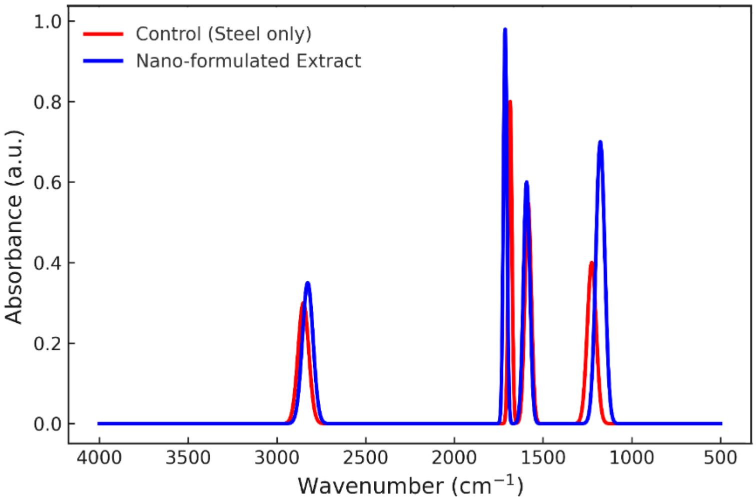

Figure 8. FTIR spectra of carbon steel in 1.0 M HCl solution in the absence (control) and presence of Piper nigrum extract encapsulated within PLGA nanoparticles

3.7. Theoretical Evaluation of Inhibitor Performance

The electronic properties of an inhibitor provide essential insights into its inhibition mechanism and adsorption tendencies on metallic surfaces. Such parameters serve as powerful tools not only for interpreting experimental findings but also for clarifying the nature of inhibitor–metal interactions. In this study, quantum chemical calculations were carried out using the DMol³ Energy/EPS package. The analysis included electrostatic potential surface (EPS) mapping, Mulliken charge distribution, Fermi level, and the frontier molecular orbital energies (HOMO and LUMO). Based on these results, several global reactivity descriptors were derived, including the HOMO–LUMO energy gap (ΔE), electronegativity (χ), softness (s), ionization energy (IE), electron affinity (EA), hardness (η), chemical potential (ρ), the fraction of electrons transferred (ΔN), and the back-donation energy ($\Delta E_{\text{Back-donation}}$). The energy gap and electronegativity were determined using Equations (7) and (8), respectively.

$$\Delta E_{gap}=E_{LUMO}-E_{HOMO} \quad (7)$$

$$x=\frac{E_{LUMO}+E_{HOMO}}{2} \quad (8)$$

Ionization energy IE and electron affinity EA were calculated by Equations 9 and 10, respectively.

$$IE=-E_{HOMO} \quad (9)$$

$$EA=-E_{LUMO} \quad (10)$$

The softness (s) and hardness (η) were calculated by Equations 11 and 12, respectively.

$$s=\frac{1}{\eta} \quad (11)$$

$$\eta=\frac{IE-AE}{2} \quad (12)$$

Chemical potential represents the first derivative of energy and was calculated through Equation 13.

$$\rho=-x \quad (13)$$

The number of transferred electrons was calculated through Equation 14:

$$\Delta N=\frac{(x_{Fe}-x_{inh})}{2(\eta_{Fe}-\eta_{inh})} \quad (14)$$

where χ_{Fe} is the absolute electronegativity of iron, and χ_{inh} denotes the absolute electronegativity of inhibitor molecules, while η_{Fe} denotes the absolute hardness of iron and ηinh denotes the absolute hardness of inhibitor molecules.

In this regard, the χ_{Fe} equals 7 eV, and ηFe equals 0 eV, and depending on these facts, the ΔN can be calculated through Equation 15:

$$\Delta N=\frac{7-\chi_{inh}}{2(\eta inh)} \quad (15)$$

As for the $\Delta E_{Back\text{-}donation}$, it was calculated through the relation with global hardness, as shown in Equation 16:

$$\Delta E_{Back-donation}=\frac{-\eta}{4} \quad (16)$$

The frontier molecular orbitals, namely the Highest Occupied Molecular Orbital (HOMO) and the Lowest Unoccupied Molecular Orbital (LUMO), are key descriptors of the electronic structure and play a crucial role in assessing the inhibition potential of organic compounds (Figure 9). To gain insight into the inhibition mechanism, quantum chemical calculations based on density functional theory (DFT) were performed. Several global reactivity descriptors, including the energy gap (ΔE_{gap}), hardness (η), softness (S), ionization energy (IE), electron affinity (EA), chemical potential (μ), electronegativity (χ), number of transferred electrons (ΔN), and back-donation energy ($\Delta E_{back\text{-}donation}$), were determined (Table 5) [39-45].

Table 5. Electronic characteristics of the inhibitor

Quantum chemical parameter	**Values**
HOMO	-4.62
LUMO	-6.17
Energy gap (ΔE_{gap})	1.55
$\Delta E_{\text{Back-donation}}$	-0.19
Number of transferred electrons ΔN	1.03
Electronegativity (χ)	5.40
Softness (s)	1.28
Hardness (η)	0.77
Ionization energy (IE)	6.17
Electron affinity (EA)	4.62
Chemical potential (ρ)	-5.40

The ability of an inhibitor molecule to act as an electron donor is determined by a combination of frontier orbital energies and derived conceptual DFT descriptors. In corrosion inhibition theory, a higher (less negative) HOMO energy reflects the molecule's tendency to donate electrons to the vacant d-orbitals of the metal surface, while a lower LUMO energy reflects the ability to accept electrons from the metal surface. The HOMO–LUMO energy gap (ΔE) serves as an indicator of molecular reactivity and charge-transfer facility. The effective electron donors typically exhibit a relatively high HOMO energy, a small ΔE, low global hardness, high softness, and a positive electron transfer number (ΔN). Importantly, a small ΔE facilitates charge transfer and enhances molecular reactivity. Previous density functional theory (DFT) studies on organic corrosion inhibitors have shown that ΔE values below ~2 eV are generally associated with strong donor–acceptor interactions and effective adsorption on steel surfaces. In our case, the calculated $\Delta E \approx 1.55$ eV confirms that the molecule possesses sufficient softness and reactivity to donate electrons to the Fe(110) surface, which is consistent with the experimentally observed increase in charge transfer resistance and reduction in corrosion current density. In the present study, the inhibitor shows a HOMO energy of −4.62 eV, a small energy gap ($\Delta E \approx 1.55$ eV), low hardness ($\eta \approx 0.77$ eV), high softness ($\sigma \approx 1.28$ eV^{-1}), and a positive ΔN value, all of which collectively confirm its strong electron-donating capability. This interpretation is fully consistent with established conceptual DFT and corrosion inhibition literature, where electron donation is assessed through these combined descriptors, and the inhibitor is capable of electron donation based on the established criterion of a small HOMO–LUMO gap and favorable HOMO positioning relative to the metal orbitals. [46-49].

<table>
<tr><td colspan="2">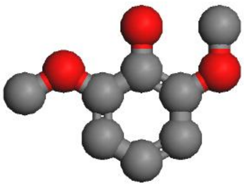 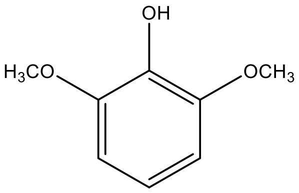 </td></tr>
<tr><td>F</td><td>Molecular structures Chemicals</td></tr>
<tr><td colspan="2">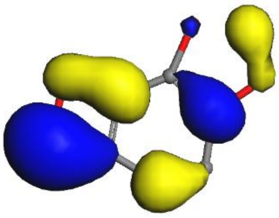 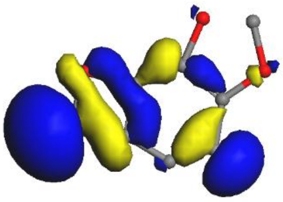</td></tr>
<tr><td>HOMO</td><td>LOMO</td></tr>
</table>

Figure 9. HOMO and LUMO orbitals of the F surfactant

In conceptual density functional theory (DFT), global hardness (η) and softness (σ) are reciprocal descriptors defined as $\eta = (E_{LUMO} - E_{HOMO})/2$ and $\sigma = 1/\eta$. A molecule is considered soft when it exhibits a relatively small hardness value (typically < 2 eV) and correspondingly high softness (> 0.5 eV^{-1}), which indicates high polarizability and ease of charge transfer. This criterion has been widely applied in corrosion inhibition studies, where soft molecules with low η and high σ values are more reactive and readily donate electrons to the vacant d-orbitals of Fe, thereby forming stable chemisorptive bonds. In our system, the calculated $\eta \approx 0.77$ eV and $\sigma \approx 1.28$ eV^{-1} fall well within the accepted range for soft inhibitors, confirming the strong donor character of the molecule. This interpretation is consistent with previous reports that classify inhibitors with $\eta < 2$ eV and $\sigma > 0.5$ eV^{-1} as soft and highly effective electron donors. Hence, the calculated hardness (0.7755 eV) and softness (1.2894 eV) further imply that the molecule is relatively soft, favoring electron donation and thereby improving its inhibitive behavior [46,47].

In addition, the ionization energy values were found to be higher than the electron affinity values, but the relatively low magnitude of ionization energy supports facile electron release. The $\Delta E_{back\text{-}donation}$ value of −0.1938 eV for molecule F reflects its ability to establish donor–acceptor interactions with the iron surface, reinforcing its adsorption tendency. Overall, the DFT results presented in Table 5 demonstrate that the inhibitor exhibits strong inhibition efficiency, in good agreement with the experimental findings [50–54].

3.8. Electrostatic Potential Surface (EPS) Analysis

Electrostatic potential mapping provides valuable insights into the distribution of electron density over atoms within a molecule. In simple terms, it distinguishes neutral, electron-rich (negative), and electron-deficient (positive) regions. Electrophilic species are more likely to interact with negatively charged areas, while nucleophilic species are inclined to attack positively charged sites. Thus, the electrostatic potential highlights how molecular structure governs inhibition efficiency. As depicted in Figure 10, variations in electrostatic potential are illustrated by distinct color gradients, corresponding to positive, negative, and neutral regions on the molecular surface. Based on the electrostatic potential values and fitted point charges, the studied inhibitor molecule displayed negative potential around oxygen atoms (−0.00056 e, −0.00065 e, and −0.00116 e) as well as on most carbon atoms, indicating their role as nucleophilic centers through adsorption on the N80 steel surface. Conversely, three carbon atoms exhibited positive potential values, suggesting localized electrophilic centers. A complete summary of these results is provided in Table 6 [55-58].

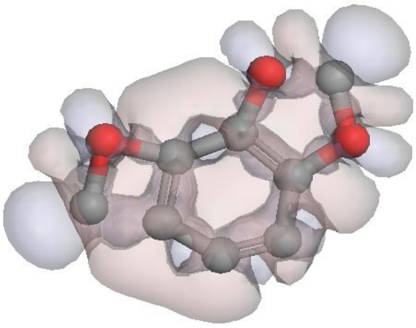

Figure 10. The molecular electrostatic potential surface and total density of molecule F

Table 6. Electrostatic potential values V(r) and their fitting electrostatic point charges of the inhibitor atom

Inhibitor molecule		
Atoms	**Charge (e)**	**V(r) (a.u)**
C	-0.00206	-1.4822
C	-0.00113	-1.9502
C	-0.00098	0.2450
C	0.00001	2.5713
C	-0.00176	2.9588
C	-0.00196	0.9126
O	-0.00056	1.9678
O	-0.00065	5.1245
C	0.00083	4.5349
O	-0.00116	-4.0997
C	0.00086	-4.7073

3.9. Molecular dynamics simulation results and analysis

To complement the static quantum chemical analysis and provide time-dependent insight into the inhibitor–metal interaction, molecular dynamics (MD) simulation was employed as a validation tool. MD simulations are widely used in corrosion science to elucidate adsorption stability, molecular orientation, surface coverage, and energetic evolution at the inhibitor–metal interface under realistic thermodynamic conditions, extending beyond static DFT predictions, thereby complementing static DFT calculations [59,60].

MD simulations provided time-dependent validation of the inhibitor–metal interactions, complementing static DFT calculations. The production trajectories revealed that both piperine and PLGA-encapsulated systems maintained stable adsorption configurations throughout the 500 ps run. The average adsorption distance between heteroatom active sites (O, N) and Fe surface atoms remained within 2.1–2.4 Å, consistent with chemisorptive binding. Calculated adsorption energies fluctuated narrowly around -172 ± 15 $kJ \cdot mol^{-1}$, confirming a spontaneous and thermodynamically favorable adsorption process. Importantly, no desorption events were observed, indicating strong interfacial stability (Figure S5).

The inhibitor adopted a nearly planar orientation on the metal surface, maximizing surface coverage and facilitating displacement of interfacial water molecules. Root mean square deviation (RMSD) analysis revealed minimal conformational fluctuation after equilibration, while radial distribution function (RDF) profiles analysis exhibited pronounced peaks at ~2.2 Å, confirming strong local interactions between heteroatoms (O, N) and Fe surface atoms. Mean square displacement (MSD) analysis demonstrated restricted molecular mobility parallel to the surface and negligible perpendicular displacement, further supporting persistent adsorption consistent with chemisorptive behavior (Figure S1-4).

The dynamic adsorption stability observed in the MD simulation correlates well with the DFT-derived electronic descriptors, including the small HOMO–LUMO energy gap ($\Delta E \approx 1.55$ eV), low global hardness ($\eta \approx 0.77$ eV), high softness ($\sigma \approx 1.28$ eV^{-1}), and positive electron transfer number ($\Delta N \approx 1.03$). Moreover, the formation of a persistent inhibitor layer supports the experimentally observed increase in charge-transfer resistance and reduction in corrosion current density. This adsorption geometry and dynamic stability further corroborate the soft molecular character of the inhibitor, as predicted by conceptual DFT and Pearson's HSAB theory. The absence of desorption events during the simulation confirms the persistence of the protective layer, which aligns with the experimentally observed increase in charge-transfer resistance and reduced corrosion current density [59,60].

Overall, the fully parameterized MD simulation confirms that the inhibitor forms a stable, energetically favorable, and dynamically persistent protective film on the metal surface. The strong agreement between MD-derived parameters, DFT calculations, and electrochemical experimental results highlights the robustness and internal consistency of the proposed corrosion inhibition mechanism.

4. CONCLUSION

In conclusion, the comprehensive experimental and theoretical investigations unequivocally confirmed the remarkable efficiency of Piper nigrum extract, particularly in its PLGA-encapsulated form, as a sustainable corrosion inhibitor for carbon steel in 1.0 M HCl. Electrochemical analyses revealed that at 50 ppm, the inhibition efficiency exceeded 92.5% at 25 °C, 91% at 35 °C, and 88.7% at 45°C, while corrosion current density values decreased drastically from 3.60×10^{-4} A/cm² (blank) to 2.69×10^{-5} A/cm² at optimal concentration, corresponding to a reduction in corrosion rate from 4.227 mm/y to 0.0096 mm/y. Complementary EIS results further validated these findings, showing a progressive increase in charge transfer resistance from 16.98 $\Omega\cdot$cm² (uninhibited) to 121.0 $\Omega\cdot$cm² at 50 ppm, alongside a concomitant decline in double-layer capacitance, confirming compact film formation. Surface characterizations (SEM, TEM, EDS, FTIR) demonstrated the uniform adsorption of phytochemicals and enhanced film compactness in the nanoencapsulated system, while theoretical DFT/MD simulations highlighted favorable adsorption energetics with adsorption energies -172 ± 15 kJ·mol^{-1} and a narrow HOMO–LUMO gap (1.55 eV), indicative of strong donor–acceptor interactions. Collectively, the findings substantiate that nanoencapsulation not only enhances adsorption stability and surface coverage but also imparts thermal robustness, rendering Piper nigrum-based nanoinhibitors a viable, eco-friendly alternative for corrosion mitigation in aggressive acidic environments.

Declarations of interest

The authors declare no conflict of interest in this reported work.

REFERENCES

[1] J.K.E. Emmanuel, Bull. Natl. Res. Cent. 48 (2024) 26.

[2] M. Bagherzadeh, and Z.S. Ghahfarokhi, Smart Anticorros. Mater. (2023) 159.

[3] M. Bagherzadeh, H. Haddadi, and M. Iranpour, Prog. Org. Coat. 101 (2016) 149.

[4] Z. Shams Ghahfarokhi, M. Bagherzadeh, E. Ghiamati Yazdi, and A. Teimouri, Anti-Corros. Methods Mater. 65 (2018) 249.

[5] E.G. Yazdi, Z.S. Ghahfarokhi, and M. Bagherzadeh, New J. Chem. 41 (2017) 12470.

[6] M. Bagherzadeh, and F. Jaberinia, J. Alloys Compd. 750 (2018) 677.

[7] NACE Int. Rep., Houston, TX (2020).

[8] H. Abdelshafeek, and A. El-Shamy, J. Mol. Liq. 383 (2023) 122110.

[9] J.K.E. Emmanuel, Bull. Natl. Res. Cent. 48 (2024) 26.

[10] C. Verma, E.E. Ebenso, and M.A. Quraishi, Sustain. Chem. 4 (2023) 321-338.

[11] S.K. Sharma, and A. Kumar, Corros. Rev. 41 (2023) 125.

[12] A. Carmona-Hernandez, M.C. Barreda-Serrano, H.A. Saldarriaga-Noreña, R. López-Sesenes, J.G. González-Rodríguez, et al., Molecules 29 (2024) 5243.
[13] A.J. Mwakalesi, Biointerface Res. Appl. Chem. 13 (2022) 32.
[14] Q. Wang, Q. Zhang, L. Liu, H. Zheng, X. Wu, Z. Li, P. Gao, Y. Sun, Z. Yan, and X. Li, J. Mol. Struct. 1265 (2022) 133367.
[15] A. Singh, and M.A. Quraishi, J. Mol. Struct. 1285 (2023) 135479.
[16] M. Faiz, A. Zahari, K. Awang, and H. Hussin, RSC Adv. 10 (2020) 6547.
[17] L. Gorgani, M. Moham, G.D. Najafpour, and M. Nikzad, Compr. Rev. 16 (2017) 124.
[18] T.K. Lim, Edible Medicinal and Non-Medicinal Plants, Springer, Dordrecht (2012) Vol. 4, pp. 322.
[19] N. Ahmad, H. Fazal, B.H. Abbasi, S. Farooq, and M. Ali, Asian Pac. J. Trop. Biomed. (2012) S1945.
[20] F. Gu, F. Huang, G. Wu, and H. Zhu, Molecules 23 (2018) 370.
[21] S. Manoharan, S. Balakrishnan, V. Menon, L. Alias, and A. Reena, Singapore Med. J. 50 (2009) 139.
[22] S.B. Nikhal, and P.A. Dambe, Hydroalcoholic Extraction of Mangifera indica Leaves by Soxhletion (2010).
[23] W.R.S. Morais, J.S. Silva, N.M.P. Queiroz, C.L.P.S. Zanta, A.S. Ribeiro, and J. Tonholo, Appl. Sci. 13 (2023) 7482.
[24] S. Fu, X. Yang, Y. Peng, Q. Wang, Q. Sun, J. Zhang, X. Wang, Z. Liang, and J. Li, Coatings 13 (2023) 613.
[25] V. Pinto, G.M. Pinto, L.D. Kateel, and A. Thomas, Biointerface Res. Appl. Chem. 13 (2023) 544.
[26] M.J. Meften, and A.A. Kadhim, J. Basrah Res. Sci. 49 (2023) 126.
[27] M.H. Hussin, and M.J. Kassim, J. Phys. Sci. 21 (2010) 1.
[28] M. Lebrini, in: J. Ou (Ed.), Corrosion Engineering: Recent Breakthroughs and Innovative Solutions, IntechOpen (2024).
[29] J.-Y. Chen, X.-B. Chen, J.-L. Li, B. Tang, N. Birbilis, and X. Wang, J. Mater. Chem. A 12 (2024) 2051.
[30] A. Toghan, M. Khairy, M. Huang, and A.A. Farag, Int. J. Electrochem. Sci. 18 (2023) 100072.
[31] C.U.D. Eze, N.A. Madueke, N.B. Iroha, N.J. Maduelosi, L.A. Nnanna, V.C. Anadebe, and A.A. Chokor, Egypt. J. Pet. 31 (2022) 31.
[32] L.B. Furtado, G.B. Leoni, R.C. Nascimento, P.H.C. Santos, F.J.F.S. Henrique, M.O.C. Guimarães, and S.L.C. Brasil, Mater. Res. 26 (2023) 1.
[33] A. Toghan, A. Fawzy, A.I. Alakhras, M.M.S. Sanad, M. Khairy, and A.A. Farag, Metals 13 (2023) 862.
[34] K. Azizollah, Iran. J. Chem. Chem. Eng. 42 (2023) 1.

[35] M.J. Meften, W.A. Radhi, and A.N. Abulhail, J. Basrah Res. Sci. 36 (2018) 1.

[36] M.J. Meften, A.A. Kadhim, A.S. Abdulnabi, and J.K. Al-zyadi, Int. J. Corros. Scale Inhib. 14 (2025) 38.

[37] P. Barman, S. Hazarika, K. Roy, R.K. Rawal, and R. Konwar, Inflammopharmacology 33 (2025) 3255.

[38] K. Shalabi, H.M. Abd El-Lateef, M.M. Hammouda, A.M.A. Osman, A.H. Tantawy, and M.A. Abo-Riya, Matererials 16 (2023) 5192.

[39] R. Jalab, M.A. Saad, M.H. Sliem, A.M. Abdullah, and I.A. Hussein, Molecules 27 (2022) 6414.

[40] L.B. Furtado, G.B. Leoni, R.C. Nascimento, P.H.C. Santos, F.J.F.S. Henrique, M.J.O.C. Guimarães, and S.L.D.C. Brasil, Mater. Res. 26 (2023) 1.

[41] M.S. Numin, K. Jumbri, K.E. Kee, A. Hassan, N. Borhan, and J. Matmin, Polymers 15 (2023) 2155.

[42] S. Fu, X. Yang, Y. Peng, Q. Wang, Q. Sun, J. Zhang, X. Wang, Z. Liang, and J. Li, Coatings 13 (2023) 613.

[43] A. Toghan, A. Fawzy, A.I. Alakhras, M.M.S. Sanad, M. Khairy, and A.A. Farag, Metals 13 (2023) 862.

[44] A. Mohammed, A.Y.I. Rubaye, W.K. Al-Azzawi, and A. Alamiery, Prog. Color, Color. Coat. 16 (2023) 347.

[45] O.E. Oyeneyin, N.D. Ojo, N. Ipinloju, E.B. Agbafa, and A.V. Emmanuel, BJBAS 11 (2022) 132, 1.

[46] N.Z.K. Razali, N.H. Mohd Noor, and N. Yahya, Chemical Papers 78 (2024) 715.

[47] A.H. Radhi, A.A. Al-Dulaimi, and A.H. Al-Janabi, NeuroQuantology 18 (2020) 37.

[48] R.G. Parr, and R.G. J. American Chem. Soc. 105 (1983) 7512.

[49] I.B. Obot, E.E. Ebenso, and D.D. Macdonald, Electrochim. Acta 134 (2014) 36.

[50] A. Bouoidina, F. El-Hajjaji, A. Abdellaoui, Z. Rais, M.F. Baba, M. Chaouch, and M. Taleb, J. Mater. Environ. Sci. 8 (2017) 1328.

[51] P. Udhayakala, Der Pharma Chem. 7 (2015) 11.

[52] S.A. Hiswa, and D.T. Alkanabi, J. Chem. Pharm. Res. 8 (2016) 65.

[53] E.G. Demissie, S.B. Kassa, and G.W. Woyessa, Int. J. Sci. Eng. Res. 5 (2014) 304.

[54] P. Udhayakalaa, T.V. Rajendiranb, and S. Gunasekaran, J. Adv. Sci. Res. 4 (2013) 31.

[55] A.H. Al-Moubaraki, A. Chaouiki, J.M. Alahmari, W.A. Al-hammadi, E.A. Noor, A.A. Al-Ghamdi, and Y.G. Ko, Materials 15 (2022) 8688.

[56] G. Bharathy, J.C. Prasana, V.S.J. Reeda, M. Prasath, and A. Manikandan, Chem. Phys. Impact 8 (2024).

[57] M.S. Shihab, and A.F. Mahmood, Port. Electrochim. Acta 35 (2017) 39.

[58] M.J. Meften, Univ. Thi-Qar, J. Sci. 7 (2019) 103.

[59] El. Azzouzi M, A. Chikh Z, and B. Hammouti, Anal. Bioanal. Electrochem. 17 (2025) 145.

[60] M. Kenzhegalieva, A. Serikbaeva, and A. Kurmanbayeva, Anal. Bioanal. Electrochem. 16 (2024) 1023.